
Interpretable Graph Learning Over Sets of Temporally-Sparse Data

Andrea Zerio^{1*} Maya Bechler-Speicher^{2*} Maor Huri²

Marie Vibeke Vestergaard¹ Ran Gilad-Bachrach²

Tine Jess^{1,3} Samir Bhatt^{4,5} Aleksejs Sazonovs¹

¹Center of Excellence for Molecular Prediction of IBD, PREDICT,

Department of Clinical Medicine, Aalborg University

²Blavatnik School of Computer Science, Tel-Aviv University

³Department of Gastroenterology & Hepatology, Aalborg University Hospital

⁴University of Copenhagen ⁵Imperial College London

*

Abstract

Real-world medical data often includes measurements from multiple signals that are collected at irregular and asynchronous time intervals. For example, different types of blood tests can be measured at different times and frequencies, resulting in fragmented and unevenly scattered temporal data. Similar issues of irregular sampling of different attributes occur in other domains, such as monitoring of large systems using event log files or the spread of fake news on social networks. Effectively learning from such data requires models that can handle sets of temporally sparse and heterogeneous signals. In this paper, we propose Graph Mixing Additive Networks (GMAN), a novel and interpretable-by-design model for learning over irregular sets of temporal signals. Our method achieves state-of-the-art performance in real-world medical tasks, including a > 4 point increase in the AUROC score of in-hospital mortality prediction, compared to existing methods. We further showcase GMAN’s flexibility by applying it to a fake news detection task. We demonstrate how its interpretability capabilities, including node-level, graph-level, and subset-level importance, allow for transition phases detection, and gaining medical insights with real-world high-stakes implications. Finally, we provide theoretical insights on GMAN expressive power.

1 Introduction

Modern clinical data consist of diverse types of measurements, often collected at irregular and asynchronous time intervals. For example, a patient’s medical record often includes a set of blood tests taken over their lifetime, where each type of test is performed at its own frequency (e.g., inflammatory markers during one visit, liver function markers two years later, followed by a repeat of inflammatory markers that same year). As a result, the data can be effectively viewed as a set of sparse temporal trajectories. Similar patterns occur in other domains. For instance, the spread of a news article may follow distinct trajectories across platforms such as X (Twitter), Facebook, or WhatsApp, each governed by its own timing, user interactions, and propagation dynamics. Each such trajectory not only follows its own temporal dynamics but also reflects the underlying relational structure of the social network through which it propagates. As another example, software event logs often contain different types of events occurring at varying times and rates.

*These authors contributed equally to this work.

To learn prediction tasks over such data, conventional approaches often rely on imputation [7, 42, 47, 13] to flatten or regularize temporally irregular data into fixed-size representations. A common strategy is to align observations to a uniform time grid and fill in missing values using interpolation or learned imputation models. Alternatively, event-based data may be transformed into sequences of inter-event intervals or cumulative event counts. Such preprocessing imposes constraints that can potentially lose informative content, risks losing the conditional dependence structure of previous events, and ignore the natural set structure of the data, where each example contains a collection of related but non-synchronized temporal sequences.

In this paper, we introduce Graph Mixing Additive Networks (GMAN), a novel framework designed to learn directly from sets of sparse, irregular temporal trajectories. We handle irregular sampling by representing each trajectory as a directed graph and modelling the entire dataset as a set of such graphs, which may differ in size and the underlying information they represent. Our approach extends Graph Neural Additive Networks (GNAN) [4], which are interpretable by design but constrained by their restriction on non-linear feature interactions, limiting expressive power. In contrast, GMAN offers a flexible trade-off between interpretability and expressive power, overcoming GNAN’s constraints. Additionally, while GNAN operates only on single graphs, GMAN supports learning from sets of graphs, enabling further interpretability through analysis of the relative importance of individual graphs within the set.

We demonstrate the effectiveness of GMAN on real-world medical datasets, where it achieves state-of-the-art (SoTA) performance with substantial margins, while also providing valuable clinical and biological insights through its interpretability features. Additionally, we evaluate GMAN on a fake news detection task, showing that it generalizes well to sets of highly diverse and complex graphs and achieves SoTA results in this domain as well. Finally, we provide a theoretical analysis proving that GMAN is strictly more expressive than GNAN, and that the proposed mechanism for balancing interpretability and expressivity leads to strictly higher expressivity compared to models that enforce full interpretability.

Our main contributions are as follows:

1. We introduce GMAN, a novel interpretable and flexible method for learning over sets of sparse, irregular temporal trajectories.
2. We demonstrate the effectiveness of GMAN on real-world medical data and fake-news detection, providing SoTA performance, including a > 4 point increase in the AUROC score of predicting in-hospital mortality, and almost 2 points increase in the AUROC score of predicting Crohn’s Disease onset.
3. We demonstrate how GMAN can provide real clinical insights with high-stake implications, through various interpretability capabilities, including node-level, graph-level, and subset-level importance scores.
4. We provide a theoretical analysis on the expressive power of GMAN.

2 Related work

Graph Neural Additive Networks Graph Neural Networks (GNNs) [24, 16, 44, 50] have become the dominant framework for learning over graph-structured data, enabling flexible representation learning across diverse domains such as healthcare [31, 30, 33], chemistry [35, 23] and social networks [25, 39], amongst others. GNNs leverage both the graph topology and node features to compute learned representations for individual nodes or for entire graphs. Recently, Bechler-Speicher et al. [4] introduced Graph Neural Additive Networks (GNANs) a novel interpretable-by-design graph learning framework inspired by generalized additive models (GAMs) [19, 20]. GNAN applies univariate neural networks to each feature of the nodes separately, and then linearly combines their outputs across nodes to produce node-level and graph-level representations. As features are not mixed non-linearly, GNAN is fully interpretable, and provides feature-level and node-level interpretability which shows exactly how each feature and each node contribute to the final target variable.

Learning from irregularly sampled trajectories In many real-world settings, data is recorded as irregularly sampled trajectories with missing values from non-uniform timing and variable feature availability. Recurrent models [7] treat missing data as latent variables, while attention-based

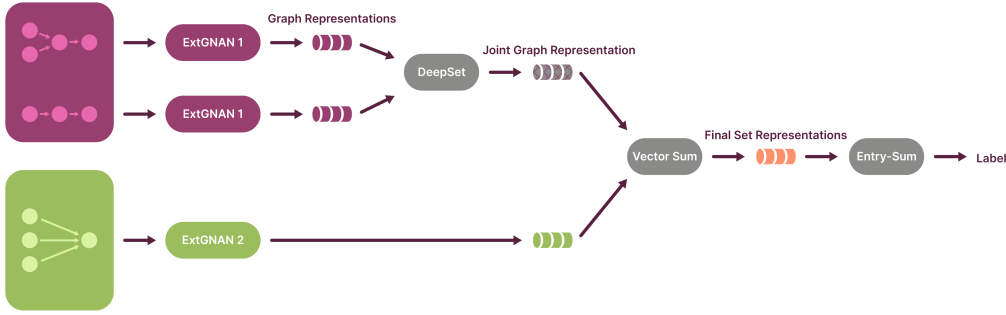


Figure 1: Overview of GMAN architecture. Each input is a set of graphs, an ExtGNAN is applied to each graph to obtain graph-level representations. Graphs can optionally be grouped and aggregated using a DeepSet module, allowing non-linear combination of related signals. This design enables a flexible trade-off between interpretability and expressivity.

methods [13, 47] reconstruct them via contextual masking and temporal blocks. Diffusion models [42, 2, 38, 12] learn conditional distributions over missing values using score-based processes. Graph-based approaches use GNNs to model feature-time dependencies through bipartite graphs, adaptive message passing, or spatio-temporal attention [52, 11, 26, 51, 9]. Despite strong reconstruction, imputation pipelines often distort dynamics and may not improve prediction [34]. An alternative is to model sparsity directly. Neural and Latent ODEs [10, 36] address irregular gaps via continuous dynamics but are compute-intensive and rely on missingness encodings. Recent models [54] instead use graph representations to capture temporal sparsity without imputation.

3 Graph Mixing Additive Networks

In this section, we present GMAN, an interpretable and flexible method for effectively learning over sets of trajectories of varying size. Let $S = \{G_1, \dots, G_m\}$ be a set of m graphs. Each node v is associated with a feature vector $x_v \in \mathbb{R}^d$ and a time-stamp t_v . For instance, in the case of a patient’s blood test data, each graph corresponds to a specific biomarker, and each node within the graph represents an individual measurement of that biomarker, annotated with its feature vector and time of collection. We denote the entry c of a vector \mathbf{h} by $[\mathbf{h}]_c$, and the set of entries corresponding to a set of features S by $[\mathbf{h}]_S$.

We assume that the graphs in S are partitioned into $k, 1 \leq k \leq m$ disjoint subsets S_k such that $\bigcup_{i=1}^k S_i = S$. The partition $\{S_i\}_{i=1}^k$ provides a flexible trade-off between expressivity and interpretability. GMAN linearly aggregates representations of the subsets of S to form a final set representation, and then assigns a single label to S . The level of interpretability that GMAN provides for each graph depends on the size of the subset it belongs to. When a subset contains a single graph, GMAN offers fine-grained, node-level importance scores. In contrast, for larger subsets, it provides only set-level importance scores—trading interpretability for improved expressivity. This design enables a flexible trade-off between interpretability and expressive power, controlled by the chosen partitioning strategy.

A visual overview of GMAN is presented in Figure 1. First, GMAN applies a function Φ_i to each subset S_i to obtain a representation of the subset S_i , denoted as $\mathbf{h}_i \in \mathbb{R}^d$.

$$\mathbf{h}_i = \Phi_i(S_i),$$

Then, it produces a representation for the whole set, \mathbf{h}_S by summing the subsets’ $\mathbf{h}_S = \sum_{i=1}^k \mathbf{h}_i$. Finally, to produce the label, it sums over the d entries of \mathbf{h}_S . Overall:

$$\text{GMAN}(S) = \sum_{c=1}^d \sum_{i=1}^k [\Phi_i(S_i)]_c \quad (1)$$

Where $\Phi_i(S_i) = \mathbf{h}_{S_i}$ is a representation of the subset S_i .

For subsets of size one, $\Phi_i(S_i)$ applies an Extended GNAN (EXTGNAN), as described in Section 3.1. For subsets containing multiple graphs, a featuregroupnan is applied to each graph, followed by a DeepSet aggregation [53] over the resulting vectors. Importantly, each subset is assigned its own EXTGNAN, and all graphs within a subset share the same one. A DeepSet first applies a neural network $f : \mathbb{R}^d \rightarrow \mathbb{R}^d$ for each vector in the set $\{h_l\}_{G_l \in S_i}$, sums the results, and then applies another neural network $g : \mathbb{R}^d \rightarrow \mathbb{R}^d$.

$$g \left(\sum_{i \in S_2} f(h_i) \right)$$

Here, g and f are neural networks of arbitrary depth and width. We now turn to define EXTGNAN.

3.1 ExtGNAN

In GNAN, univariate neural networks are applied to each feature of each node in isolation, to learn a representation for a graph. This has the benefit of generating interpretable models as features do not mix non-linearly. Nonetheless, when interactions between features are crucial for the task, it may result in sub-par performance. Therefore, EXTGNAN extends GNAN by allowing multivariate neural networks to operate on groups of features to gain accuracy at the cost of reducing the feature-level interpretability of the model.

Assume that the features are partitioned into K subsets $\{F_l\}_{l=1}^K$. For any subset of features greater than one, EXTGNAN applies a multivariate neural network for all the features in the subset together, instead of a univariate neural network for each one separately. To learn a representation of a graph G , EXTGNAN first computes representations for the nodes of G as follows.

EXTGNAN learns a distance function $\rho(x; \theta) : \mathbb{R} \rightarrow \mathbb{R}$ and a set of feature shape functions $\{\psi_l\}_{l=1}^K, \psi_l(X; \theta_k) : \mathbb{R}^{|F_l|} \rightarrow \mathbb{R}^{|F_l|}$. Each of these functions is a neural network of arbitrary depth. For brevity, we omit the parameterization θ and θ_k for the remainder of this section.

The entries of the representation of node j corresponding to the indices of the features in F_l , denoted as $[\mathbf{h}_j]_{F_l}$, is computed by summing the contributions of the features in the subset F_l from all nodes in the graph:

$$[\mathbf{h}_j]_{F_l} = \sum_{w \in V} \rho(\Delta(w, j)) \cdot \psi_l([\mathbf{X}_w]_{F_l}),$$

where $\Delta(w, j) = t_w - t_j$ and $[\mathbf{X}_w]_{F_l}$ are the features of node w corresponding to the subset F_l .

Overall, the full representation of node j can be written as:

$$\mathbf{h}_j = ([\mathbf{h}_j]_{F_1}, [\mathbf{h}_j]_{F_2}, \dots, [\mathbf{h}_j]_{F_K}).$$

Then EXTGNAN produces a graph representation by summing the node representations,

$$\mathbf{h}_G = \sum_{i \in V} \mathbf{h}_i. \tag{2}$$

This concludes the description of EXTGNAN, which computes graph-level representations. Next, we describe how GMAN combines these representations across sets and enables multi-level interpretability.

3.2 Node, graph and set importance

GMAN retains all interpretability properties of GNAN, including feature-level and node-level importance. However, it extends beyond GNAN by operating on sets of graphs rather than single graphs, enabling additional forms of interpretability such as graph-level and subset-level importance. Because GMAN allows a flexible trade-off between interpretability and expressivity, permitting non-linear mixing within graph subsets, some adaptations are required to extract meaningful attributions under this more expressive regime. Due to space constraints, we present only the formulations for

node and graph importance here; additional interpretability measures are provided in the Appendix. Section 4 illustrates how node-level attributions yield meaningful real-world insights.

We can extract the total contribution of each node j to the prediction by summing the contributions of the node across all feature sets. This is only valid when the node belongs to a graph that is not combined non-linearly with other graphs, i.e., it belongs to a subset of size one.

Therefore, the contribution of node j is

$$\text{TotalContribution}(j) = \sum_{l=1}^K [\mathbf{h}_j]_{F_k} = \sum_{w \in V} \rho(\Delta(w, j)) \sum_{l=1}^K \psi_k([\mathbf{x}_w]_l, l \in F_k). \quad (3)$$

The contribution of a graph G is then

$$\text{TotalContribution}(G) = \sum_{v \in G} \text{TotalContribution}(v).$$

For graphs that are mixed non-linearly, i.e., graphs that belong in subsets of size greater than one, interpretability is more limited, and we can only provide the total contribution of the set to the final prediction

$$\text{TotalContribution}(S) = \sum_{l=1}^K [\mathbf{S}]_{F_k}. \quad (4)$$

3.3 Expressivity properties

In this section we provide a theoretical analysis of the expressiveness of GMAN.

Theorem 3.1. GMAN is strictly more expressive than GNAN.

The following theorem shows that a GMAN which is applied to subsets of graphs of size at least two, is more expressive than a GMAN that is applied to only subsets of size one:

Theorem 3.2. Let S be a set of graphs $\{G_i\}_{j=1}^m$. Let $S_1 = \{S_i\}_{i=1}^m$ be a partition of S such that $|S_i| = 1$. Let $S_2 = \{S_i\}_{i=1}^k$ such that there exists k with $|S_k| > 1$. with a subset partition $\{S_i\}_{i=1}^k$. Then a GMAN trained over S_2 is strictly more expressive than a GMAN trained over S_1 .

4 Empirical evaluation

In this section, we evaluate GMAN on a diverse set of real-world tasks to assess its effectiveness across both domains and graph structures². We include two biomedical datasets: ICU mortality prediction and Crohn’s Disease (CD) diagnosis, where inputs are temporally sparse biomarker trajectories. To test performance on structurally different data, we also evaluate GMAN on a social media dataset for fake news detection, which involves more complex, densely connected graphs. This range of tasks enables a rigorous assessment of GMAN’s ability to generalize across graph structures and application settings, highlighting both its flexibility and practical relevance. Additional details on the datasets, experimental setup, and hyperparameter configurations are provided in the Appendix.

4.1 Medical predictions

We evaluate GMAN on two high-impact clinical prediction tasks: in-hospital mortality among intensive care patients and onset of Crohn’s Disease. In both settings, each individual is represented as a set of time-stamped biomarker trajectories, where each trajectory forms a directed line graph with nodes corresponding to test results and edges encoding the time elapsed between measurements. This representation preserves the temporal structure of each biomarker independently while enabling joint reasoning across biomarkers during learning. Both tasks are framed as binary classification. Importantly, the outcomes we predict carry serious clinical implications. Missed detections can

²Code implementation can be found at <http://github.com/azerio/Graph-Mixing-Additive-Networks---GMAN>

delay critical treatment, while false alarms may lead to unnecessary interventions. These results demonstrate the effectiveness of GMAN when applied to real-world clinical data and its potential for deployment in high-stakes decision-making environments.

4.1.1 In-hospital mortality prediction

Data The PhysioNet2012 (P12) dataset, introduced by [17], contains records from 11,988 ICU patients, following the exclusion of 12 samples deemed inappropriate according to the criteria in Horn et al. (2020). For each patient, time series measurements from 36 physiological signals (excluding weight) were recorded over the initial 48 hours of ICU admission. Additionally, each patient has a static profile comprising 9 features, including demographic and clinical attributes such as age and gender. The dataset is labelled for a binary classification task: predicting in-hospital mortality.

Setup We compare GMAN to other 9 baselines evaluated in [55], including: *Transformer* [43], *Trans-mean*, *GRU-D* [8], *SeFT* [22], *mTAND* [41], *IP-Net*[40], *DGM*²[48] and *MTGNN* [49]. We use the data splits as in [55], which are random splits of train (80%), validation (10%), and test (10%) set over the data. We conducted a grid search by training on the training set and evaluating on the validation set. We selected the best performing model over the validation set. We report the average AUROC score and standard-deviation of the selected configuration with 3 seeds. As input subsets for the model, we put all biomarkers in separate subsets, except for 5 biomarkers which are in the same subset. The complete subsets information is provided in the Appendix.

Results The results are presented in Table 1. GMAN achieves the highest AUROC, outperforming the next best baseline, IP-Net by 4.14 AUCROC points. Notably, while other approaches are more expressive black-box methods, GMAN achieves high performance while remaining fully interpretable.

4.1.2 Crohn’s disease prediction

Data The Danish health registries are comprehensive, nationwide databases covering healthcare interactions for over 9.5 million individuals [32]. A key resource is the Registry of Laboratory Results for Research (RLRR), which has collected laboratory test results from hospitals and general practitioners since 2015 [3]. From this data, we constructed a cohort of 8,567 individuals later diagnosed with Crohn’s Disease (CD) and 8,567 age-matched controls from the same registry. For each person, we extracted temporal trajectories of 17 routinely measured biomarkers, reflecting key physiological processes such as immune response, inflammation, organ function, and nutritional status. The only exception is faecal calprotectin (F-Cal), a stool-based biomarker specifically used to detect intestinal inflammation in conditions like CD. The complete list and descriptions of these biomarkers are provided in the Appendix. The task is binary classification: predicting future CD onset from pre-diagnostic medical histories.

Setup We randomly split the dataset into 80% training, 10% validation, and 10% test sets. GMAN is trained for up to 300 epochs, with the best model selected based on validation performance. We report the mean and standard deviation (std) of AUROC across three random seeds. We trained GMAN using 7 subsets of biomarkers of different cardinality, representing different physiological functions. Full details of the subsets are provided in the Appendix.

We compare GMAN against widely used baselines for Crohn’s Disease prediction, including Random Forest (RF) [21] and Gradient Boosting (GB) [14], which are strong performers on structured biomedical data [15, 45, 37]. We also benchmark against two Transformer-based architectures, a standard *Transformer*[43] and *Trans-mean* [54]. We chose these as they act as high-capacity sequence models, designed to capture complex, long-range temporal dependencies without imposing strong

Table 1: Evaluation of GMAN on predicting in-hospital mortality over the P12 dataset.

Methods	AUROC
Transformer	65.1 ± 5.6
Trans-mean	66.8 ± 4.2
GRU-D	67.2 ± 3.6
SeFT	66.8 ± 0.8
mTAND	65.3 ± 1.7
IP-Net	72.5 ± 2.4
DGM ²	71.2 ± 2.5
MTGNN	67.5 ± 3.1
RAINDROP	72.1 ± 1.3
GMAN	76.64 ± 1.2

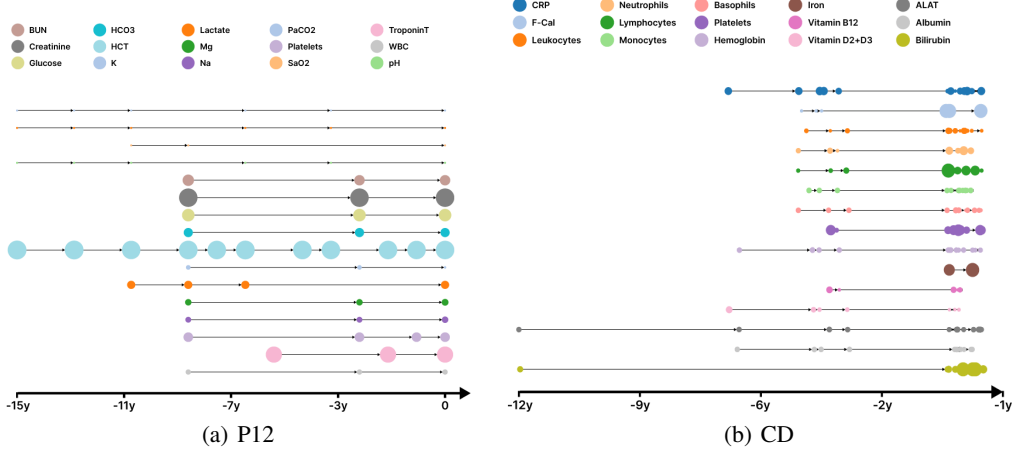


Figure 2: Node-level attributions for two individuals from (a) the P12 ICU mortality and (b) CD onset datasets. Node size indicates each measurement’s contribution to the prediction. GMAN highlights clinically relevant signals, renal and cardiac markers in P12, inflammation biomarkers in CD, demonstrating fine-grained temporal interpretability. CD data is privacy-protected via noise and temporal shifting.

parametric assumptions on the data-generating process. Because these baselines do not operate on graph-structured inputs, we revert to the original tabular format, where each row represents all biomarker tests taken on a given date, along with static features such as sex. For classical models, each row is treated as an independent example, with biomarker tuples parsed into numerical and categorical features. Categorical features are one-hot encoded, and missing values are imputed using a zero-inflation strategy.

Results We report the results of GMAN in Table 2. GMAN outperforms all baseline models, achieving a 1.9-point improvement in AUROC over the next-best method. While classical baselines such as GB and RF offer feature importance scores, GMAN provides a richer and more granular interpretability framework. In addition to feature-level insights, it supports node-level and graph-level attributions, allowing us to pinpoint which specific measurements, and which temporal patterns, most influenced the model’s prediction. These multi-scale interpretability capabilities are explored in detail in the following subsection. Additional discussion of related work on predicting Crohn’s Disease onset, using both simple blood-based biomarkers and more complex biochemical features such as multi-omics data, is provided in the Appendix.

4.1.3 Clinical insights through interpretability

Beyond predictive performance, a central strength of GMAN is that interpretability is built into the model by design, rather than added post hoc. This allows for fine-grained, temporally resolved explanations that go beyond global feature importance, enabling users to understand how and when specific biomarkers influence the model’s predictions. In high-stakes domains such as healthcare, this level of transparency is crucial. Clinical decision-making often depends not only on the outcome of a prediction but on a clear understanding of the reasoning behind it. Models that can provide such insights are far more likely to be trusted, audited, and integrated into clinical workflows. To highlight the interpretability of GMAN, we conduct attribution analyses on both the CD and P12 datasets, examining how the model assigns importance across time and features.

Table 2: Evaluation of GMAN on predicting CD onset from pre-diagnostic biomarker trajectories.

Methods	AUROC
Transformer	66.17 ± 0.3
Trans-mean	70.78 ± 2.4
Random Forest	80.76 ± 0.2
Naive Bayes	67.59 ± 1.8
GB	81.70 ± 0.3
GMAN	83.64 ± 0.9

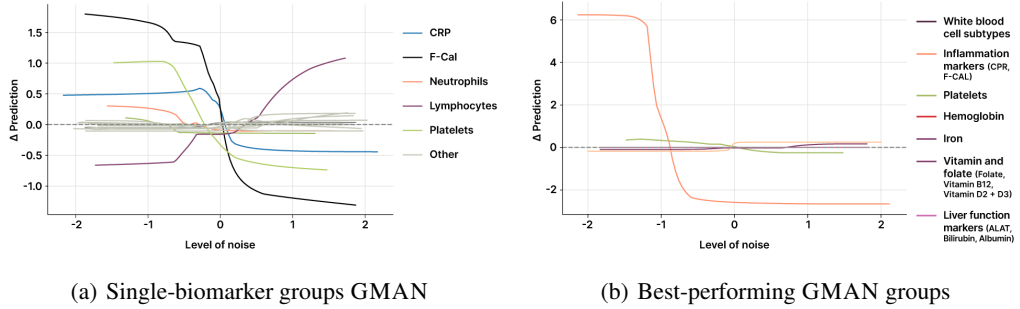


Figure 3: Subset-level contribution curves for Crohn’s Disease prediction. Each curve shows how the model’s output changes as increasing noise is added to the latent representation of a biomarker group. (a) uses individual biomarkers, revealing strong effects from F-Cal, platelets, CRP and lymphocytes. (b) uses physiologically coherent groups, where inflammation markers (CRP, F-Cal) dominate the prediction.

Critical phase detection through node-level importance In the GMAN framework, nodes represent individual measurements within a biomarker trajectory. As such, highly influential nodes can highlight critical phases where specific measurements most strongly impact the prediction. We use Equation (3) to quantify node-level contributions across biomarkers in both the CD and P12 datasets. Figure 2 displays node-level importance across biomarker trajectories for two randomly selected individuals from each dataset, with node size reflecting the magnitude of each node’s contribution to the model’s prediction. In both clinical tasks, the model’s attributions appear consistent with established biomedical knowledge. For Crohn’s Disease prediction, GMAN highlights key inflammatory and immune markers, such as faecal F-Cal, platelets, and lymphocytes, as primary contributors. All of these are known to play central roles in disease onset [45]. In the P12 example, the model assigns high importance to markers of renal function, liver injury, cardiac stress, and metabolic imbalance, aligning well with clinical predictors of poor outcomes in intensive care settings.

Total biomarker contribution In addition to node-level attributions, GMAN provides subset-level importance scores, quantifying the contribution of entire biomarker groups to the model’s prediction. This enables flexible, system-level interpretability, allowing users to assess the collective influence of physiologically related biomarkers on the target variable. We conduct a subset-level attribution analysis on the CD dataset using two clinically motivated grouping strategies. In the first, we assess individual biomarkers to determine whether the model prioritizes features known to be associated with CD onset, allowing us to verify its alignment with established biomedical knowledge. In the second, we group biomarkers into clinically coherent subsets based on physiological function, such as immune response; inflammation; oxygen transport; and liver function; to examine whether the model captures system-level patterns consistent with disease progression. Full details on the clinical significance of these groupings are provided in the Appendix. For each grouping strategy, we train a separate instance of GMAN. To quantify the importance of each biomarker subset, we use Equation (4), measuring how the model’s prediction changes as increasing amounts of noise are added to the features of nodes within that subset. To introduce noise in a structured way, we apply PCA [1] to the feature vectors of all nodes corresponding to biomarkers in the group, and progressively perturb the input along the 1st principal component. This procedure is performed independently for each subset and allows us to assess the model’s sensitivity to perturbations in biologically meaningful groupings, offering insight into the relative predictive weight of each group. Notice that as the importance of a subset is the exact value it contributes to the prediction, measuring the change in the prediction is equivalent to measuring the change in importance.

Figure 3 presents the results of the subset-level attribution analysis. In the single-biomarker setting (Figure 3(a)), F-Cal, platelets, and lymphocytes show strong directional effects on model output. F-Cal and platelets are positively associated with CD risk, while lymphocytes have an inverse effect, findings that are both biologically grounded and consistent with prior work [45]. In the clinically-coherent group setting (Figure 3(b)), the inflammation group, comprised of CRP and F-Cal,

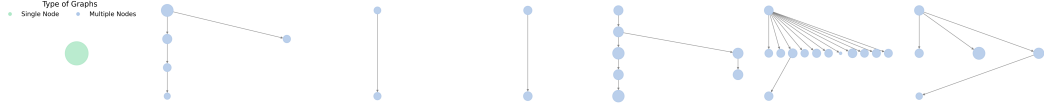


Figure 4: Node importance for fake-news spread graphs, over the GOS dataset. The node size correspond to its importance learned by the model, according to Equation (3)

emerges as the most influential, with a pronounced non-linear effect on predictions, aligning with their established diagnostic relevance in CD [45].

4.2 Fake-News Detection

Data GossipCop (GOD) is a dataset of news articles annotated by professional journalists and fact-checkers, containing both content-based labels and social context information verified through the GossipCop fact-checking platform. It is composed of 5,464 tree-structured graphs based on retweet information, where the news article is the root node and retweeting users are subsequent nodes in the cascade, with edges signifying retweet relationships. Each node in these graphs is associated with 4 features: 768-dimensional embeddings generated using a pretrained BERT model on user historical tweets, 300-dimensional embeddings from pretrained word2vec [27] on the same historical tweets, 10-dimensional features extracted from user profiles, and a 310-dimensional "content" feature that combines the 300-dimensional embedding of user comments with the 10-dimensional profile features. Each graph is labelled to indicate whether it originates from a fake news post or not. We decomposed the tree into a set of directed graphs rooted at the origin, each representing a distinct path of news propagation.

Setup We evaluated GMAN against 4 GNNs, including GATv2 [5], GraphConv [29], GraphSAGE [18] and GCNFN [28]. We use random splits of train (80%), validation (10%), and test (10%) sets over the data and selected the best performing model over the validation set. We then report the average Accuracy score and std of the selected configuration with three seeds. Since many subgraphs reduce to a single node after decomposition, we group all size-one graphs into a shared subset and combine them non-linearly. For the remaining graphs, whose identities are not uniquely distinguishable, we apply a shared EXTGNAN. In total, we use two distinct EXTGNAN modules.

Results and node-level importance Results are provided in Table 3. GMAN outperforms all baselines, with an uplift of 0.57 accuracy points.

Figure 4 presents the node importance of a random sample from the datasets, where the size of a node corresponds to its importance score according to Equation (3).

5 Conclusion

In this work, we present GMAN, a novel method that extends GNAN[4] for learning from sets of temporally sparse graphs, while allowing a flexible balance between interpretability and expressivity. We show that GMAN achieves state-of-the-art results across real-world medical predictions tasks with high-stake implications, as well as fake news detection, including over 4 AUCROC points improvement in predicting in-hospital mortality. We demonstrate how the strong interpretability capabilities of GMAN, including node-, graph-, and set-level explanations, can be leveraged to uncover novel clinical insights, such as identifying transition phases in patient disease progression. We provide a theoretical analysis of GMAN, and show it is strictly more expressive than GNAN. Overall, GMAN’s flexibility and expressiveness makes it well-suited for a wide range of real-world tasks involving irregular and heterogeneous data, particularly in domains such as healthcare where interpretability is crucial.

Table 3: Evaluation of GMAN on the Gossipcop (GOS) fake news detection dataset.

Methods	Accuracy
GATv2	96.10 ± 0.3
GraphConv	96.77 ± 0.1
GraphSage	94.45 ± 1.5
GCNFN	96.52 ± 0.2
GMAN	97.34 ± 0.2

References

- [1] Hervé Abdi and Lynne J Williams. Principal component analysis. *Wiley interdisciplinary reviews: computational statistics*, 2(4):433–459, 2010.
- [2] Juan Miguel Lopez Alcaraz and Nils Strodthoff. Diffusion-based time series imputation and forecasting with structured state space models. *arXiv preprint arXiv:2208.09399*, 2022.
- [3] Johan Frederik Håkonsen Arendt, Anette Tarp Hansen, Søren Andreas Ladefoged, Henrik Toft Sørensen, Lars Pedersen, and Kasper Adelborg. Existing data sources in clinical epidemiology: laboratory information system databases in denmark. *Clinical epidemiology*, pages 469–475, 2020.
- [4] Maya Bechler-Speicher, Amir Globerson, and Ran Gilad-Bachrach. The intelligible and effective graph neural additive network. *Advances in Neural Information Processing Systems*, 37:90552–90578, 2024.
- [5] Shaked Brody, Uri Alon, and Eran Yahav. How attentive are graph attention networks?, 2022. URL <https://arxiv.org/abs/2105.14491>.
- [6] Peter Buneman. A note on the metric properties of trees. *J. Combin. Theory Ser. B*, 17(1):48–50, 1974.
- [7] Wei Cao, Dong Wang, Jian Li, Hao Zhou, Lei Li, and Yitan Li. Brits: Bidirectional recurrent imputation for time series. *Advances in neural information processing systems*, 31, 2018.
- [8] Zhengping Che, Sanjay Purushotham, Kyunghyun Cho, David Sontag, and Yan Liu. Recurrent neural networks for multivariate time series with missing values, 2016. URL <https://arxiv.org/abs/1606.01865>.
- [9] Qianyi Chen, Jiannong Cao, Yu Yang, Wanyu Lin, Sumei Wang, and Youwu Wang. Multistage graph convolutional network with spatial attention for multivariate time series imputation. *IEEE Transactions on Neural Networks and Learning Systems*, 2024.
- [10] Ricky TQ Chen, Yulia Rubanova, Jesse Bettencourt, and David K Duvenaud. Neural ordinary differential equations. *Advances in neural information processing systems*, 31, 2018.
- [11] Andrea Cini, Ivan Marisca, and Cesare Alippi. Filling the g_ap_s: Multivariate time series imputation by graph neural networks, 2022. URL <https://arxiv.org/abs/2108.00298>.
- [12] Zongyu Dai, Emily Getzen, and Qi Long. Sadi: Similarity-aware diffusion model-based imputation for incomplete temporal ehr data. In *International Conference on Artificial Intelligence and Statistics*, pages 4195–4203. PMLR, 2024.
- [13] Wenjie Du, David Côté, and Yan Liu. Saits: Self-attention-based imputation for time series. *Expert Systems with Applications*, 219:119619, 2023.
- [14] Jerome H Friedman. Greedy function approximation: a gradient boosting machine. *Annals of statistics*, pages 1189–1232, 2001.
- [15] Manik Garg, Marcin Karpinski, Dorota Matelska, Lawrence Middleton, Oliver S Burren, Fengyuan Hu, Eleanor Wheeler, Katherine R Smith, Margarete A Fabre, Jonathan Mitchell, et al. Disease prediction with multi-omics and biomarkers empowers case–control genetic discoveries in the uk biobank. *Nature Genetics*, 56(9):1821–1831, 2024.
- [16] Justin Gilmer, Samuel S Schoenholz, Patrick F Riley, Oriol Vinyals, and George E Dahl. Neural message passing for quantum chemistry. In *International conference on machine learning*, pages 1263–1272. PMLR, 2017.
- [17] Ary L Goldberger, Luis AN Amaral, Leon Glass, Jeffrey M Hausdorff, Plamen Ch Ivanov, Roger G Mark, Joseph E Mietus, George B Moody, Chung-Kang Peng, and H Eugene Stanley. Physiobank, physiotoolkit, and physionet: components of a new research resource for complex physiologic signals. *circulation*, 101(23):e215–e220, 2000.

[18] William L. Hamilton, Rex Ying, and Jure Leskovec. Inductive representation learning on large graphs, 2018. URL <https://arxiv.org/abs/1706.02216>.

[19] Trevor Hastie and Robert Tibshirani. Generalized additive models. *Statistical science*, 1(3):297–310, 1986.

[20] Trevor Hastie and Robert Tibshirani. Generalized additive models: some applications. *Journal of the American Statistical Association*, 82(398):371–386, 1987.

[21] Tin Kam Ho. Random decision forests. In *Proceedings of 3rd international conference on document analysis and recognition*, volume 1, pages 278–282. IEEE, 1995.

[22] Max Horn, Michael Moor, Christian Bock, Bastian Rieck, and Karsten Borgwardt. Set functions for time series, 2020. URL <https://arxiv.org/abs/1909.12064>.

[23] John Jumper, Richard Evans, Alexander Pritzel, Tim Green, Michael Figurnov, Olaf Ronneberger, Kathryn Tunyasuvunakool, Russ Bates, Augustin Žídek, Anna Potapenko, et al. Highly accurate protein structure prediction with alphafold. *nature*, 596(7873):583–589, 2021.

[24] Thomas N Kipf and Max Welling. Semi-supervised classification with graph convolutional networks. *arXiv preprint arXiv:1609.02907*, 2016.

[25] Xiao Li, Li Sun, Mengjie Ling, and Yan Peng. A survey of graph neural network based recommendation in social networks. *Neurocomputing*, 549:126441, 2023.

[26] Ivan Marisca, Andrea Cini, and Cesare Alippi. Learning to reconstruct missing data from spatiotemporal graphs with sparse observations. *Advances in neural information processing systems*, 35:32069–32082, 2022.

[27] Tomas Mikolov, Kai Chen, Greg Corrado, and Jeffrey Dean. Efficient estimation of word representations in vector space. *arXiv preprint arXiv:1301.3781*, 2013.

[28] Federico Monti, Fabrizio Frasca, Davide Eynard, Damon Mannion, and Michael M. Bronstein. Fake news detection on social media using geometric deep learning, 2019. URL <https://arxiv.org/abs/1902.06673>.

[29] Christopher Morris, Martin Ritzert, Matthias Fey, William L. Hamilton, Jan Eric Lenssen, Gaurav Rattan, and Martin Grohe. Weisfeiler and leman go neural: Higher-order graph neural networks, 2021.

[30] Juan G Diaz Ochoa and Faizan E Mustafa. Graph neural network modelling as a potentially effective method for predicting and analyzing procedures based on patients’ diagnoses. *Artificial Intelligence in Medicine*, 131:102359, 2022.

[31] Showmick Guha Paul, Arpa Saha, Md Zahid Hasan, Sheak Rashed Haider Noori, and Ahmed Moustafa. A systematic review of graph neural network in healthcare-based applications: Recent advances, trends, and future directions. *IEEE Access*, 12:15145–15170, 2024.

[32] Carsten Bøcker Pedersen. The danish civil registration system. *Scandinavian journal of public health*, 39(7_suppl):22–25, 2011.

[33] Wei Peng, Tielin Chen, Hancheng Liu, Wei Dai, Ning Yu, and Wei Lan. Improving drug response prediction based on two-space graph convolution. *Computers in Biology and Medicine*, 158:106859, 2023.

[34] Linglong Qian, Yiyuan Yang, Wenjie Du, Jun Wang, Richard Dobsoni, and Zina Ibrahim. Beyond random missingness: Clinically rethinking for healthcare time series imputation, 2025. URL <https://arxiv.org/abs/2405.17508>.

[35] Patrick Reiser, Marlen Neubert, André Eberhard, Luca Torresi, Chen Zhou, Chen Shao, Housam Metni, Clint van Hoesel, Henrik Schopmans, Timo Sommer, et al. Graph neural networks for materials science and chemistry. *Communications Materials*, 3(1):93, 2022.

[36] Yulia Rubanova, Ricky TQ Chen, and David K Duvenaud. Latent ordinary differential equations for irregularly-sampled time series. *Advances in neural information processing systems*, 32, 2019.

[37] Aleksejs Sazonovs*, Kirsten Schut*, Nikolas Plevris, Filip A Ottosson, Tine Jess#, Jeffrey C Barrett#, and Charlie W Lees#. OP19 Pre-and post-diagnostic metabolomic biomarker profiling of over 700,000 individuals in three national biobanks enables prediction of inflammatory bowel disease onset and complications. *Journal of Crohn's and Colitis*, 19(Supplement_1):i38–i41, 2025. * Co-first authors. # Co-senior author.

[38] Zineb Senane, Lele Cao, Valentin Leonhard Buchner, Yusuke Tashiro, Lei You, Paweł Andrzej Herman, Mats Nordahl, Ruibo Tu, and Vilhelm Von Ehrenheim. Self-supervised learning of time series representation via diffusion process and imputation-interpolation-forecasting mask. In *Proceedings of the 30th ACM SIGKDD Conference on Knowledge Discovery and Data Mining*, pages 2560–2571, 2024.

[39] Kartik Sharma, Yeon-Chang Lee, Sivagami Nambi, Aditya Salian, Shlok Shah, Sang-Wook Kim, and Srijan Kumar. A survey of graph neural networks for social recommender systems. *ACM Computing Surveys*, 56(10):1–34, 2024.

[40] Satya Narayan Shukla and Benjamin M. Marlin. Interpolation-prediction networks for irregularly sampled time series, 2019. URL <https://arxiv.org/abs/1909.07782>.

[41] Satya Narayan Shukla and Benjamin M. Marlin. Multi-time attention networks for irregularly sampled time series, 2021. URL <https://arxiv.org/abs/2101.10318>.

[42] Yusuke Tashiro, Jiaming Song, Yang Song, and Stefano Ermon. Csd: Conditional score-based diffusion models for probabilistic time series imputation. *Advances in neural information processing systems*, 34:24804–24816, 2021.

[43] Ashish Vaswani, Noam Shazeer, Niki Parmar, Jakob Uszkoreit, Llion Jones, Aidan N Gomez, Łukasz Kaiser, and Illia Polosukhin. Attention is all you need. *Advances in neural information processing systems*, 30, 2017.

[44] Petar Veličković, Guillem Cucurull, Arantxa Casanova, Adriana Romero, Pietro Lio, Yoshua Bengio, et al. Graph attention networks. *stat*, 1050(20):10–48550, 2017.

[45] Marie Vibeke Vestergaard, Kristine H Allin, Gry J Poulsen, James C Lee, and Tine Jess. Characterizing the pre-clinical phase of inflammatory bowel disease. *Cell Reports Medicine*, 4(11), 2023.

[46] Jakob Woerner, Thomas Westbrook, Seokho Jeong, Manu Shivakumar, Allison R Greenplate, Sokratis A Apostolidis, Seunggeun Lee, Yonghyun Nam, and Dokyoon Kim. Plasma protein-based and polygenic risk scores serve complementary roles in predicting inflammatory bowel disease. In *Pacific Symposium on Biocomputing. Pacific Symposium on Biocomputing*, volume 30, page 522, 2025.

[47] Haixu Wu, Tengge Hu, Yong Liu, Hang Zhou, Jianmin Wang, and Mingsheng Long. Timesnet: Temporal 2d-variation modeling for general time series analysis. *arXiv preprint arXiv:2210.02186*, 2022.

[48] Yinjun Wu, Jingchao Ni, Wei Cheng, Bo Zong, Dongjin Song, Zhengzhang Chen, Yanchi Liu, Xuchao Zhang, Haifeng Chen, and Susan Davidson. Dynamic gaussian mixture based deep generative model for robust forecasting on sparse multivariate time series, 2021. URL <https://arxiv.org/abs/2103.02164>.

[49] Zonghan Wu, Shirui Pan, Guodong Long, Jing Jiang, Xiaojun Chang, and Chengqi Zhang. Connecting the dots: Multivariate time series forecasting with graph neural networks, 2020. URL <https://arxiv.org/abs/2005.11650>.

[50] Keyulu Xu, Weihua Hu, Jure Leskovec, and Stefanie Jegelka. How powerful are graph neural networks? *arXiv preprint arXiv:1810.00826*, 2018.

- [51] Yongchao Ye, Shiyao Zhang, and James JQ Yu. Spatial-temporal traffic data imputation via graph attention convolutional network. In *International Conference on artificial neural networks*, pages 241–252. Springer, 2021.
- [52] Jiaxuan You, Xiaobai Ma, Yi Ding, Mykel J Kochenderfer, and Jure Leskovec. Handling missing data with graph representation learning. *Advances in Neural Information Processing Systems*, 33:19075–19087, 2020.
- [53] Manzil Zaheer, Satwik Kottur, Siamak Ravanbakhsh, Barnabas Poczos, Ruslan Salakhutdinov, and Alexander Smola. Deep sets, 2018. URL <https://arxiv.org/abs/1703.06114>.
- [54] Xiang Zhang, Marko Zeman, Theodoros Tsiligkaridis, and Marinka Zitnik. Graph-guided network for irregularly sampled multivariate time series. *arXiv preprint arXiv:2110.05357*, 2021.
- [55] Xiang Zhang, Marko Zeman, Theodoros Tsiligkaridis, and Marinka Zitnik. Graph-guided network for irregularly sampled multivariate time series, 2022. URL <https://arxiv.org/abs/2110.05357>.

Appendix

6 Theoretical Framework

This section consolidates the theoretical foundations of GMAN by presenting formal proofs of its expressive power and structural recoverability guarantees. We first prove that GMAN is strictly more expressive than GNAN, both in terms of multivariate feature learning and subset level representation. We then establish conditions under which GMAN can recover the latent structure of input graphs purely from learned pairwise distances. Specifically, we show that when graphs form tree-structured trajectories, the model’s learned distance matrix implicitly determines the original graph topology, up to isomorphism.

6.1 Proof of Theorem 3.1

We will prove that GMAN is strictly more expressive than GNAN. To prove this, we use a ground truth function that is a feature-level XOR. Let a single-node graph be endowed with binary features $x = (x_1, x_2) \in \{0, 1\}^2$ and define the target $f_{\oplus}(x) = x_1 \oplus x_2$.

First we will show that GNAN cannot express f_{\oplus} . A GNAN scores the graph by $\hat{y} = \sigma(\phi_1(x_1) + \phi_2(x_2))$, where each ϕ_i is univariate. Put $a = \phi_1(0)$, $b = \phi_1(1)$, $c = \phi_2(0)$, $d = \phi_2(1)$. To match the XOR truth-table there must exist a threshold τ such that

$$a + c < \tau, \quad b + c > \tau, \quad a + d > \tau, \quad b + d < \tau.$$

Summing the first and last inequalities yields $a + b + c + d < 2\tau$, while the middle pair gives $a + b + c + d > 2\tau$ —a contradiction. Thus no GNAN realises f_{\oplus} .

Now we will show that GMAN can express f_{\oplus} . Place the two features in the same subset $F = \{x_1, x_2\}$ and choose the subset-network

$$\psi_F(x_1, x_2) = x_1 + x_2 - 2x_1x_2.$$

For the four binary inputs this mapping returns $(0, 1, 1, 0)$, exactly f_{\oplus} . Hence GMAN represents a function unattainable by GNAN, proving that GMAN is strictly more expressive.

6.2 Proof of Theorem 3.2

Let S be a set of graphs $\{G_i\}_{i=1}^m$. Let $S_1 = \{S_i\}_{i=1}^m$ be a partition of S such that $|S_i| = 1$. Let $S_2 = \{S_i\}_{i=1}^k$ such that there exists k with $|S_k| > 1$, with a subset partition $\{S_i\}_{i=1}^k$. We will prove that a GMAN trained over S_2 is strictly more expressive than a GMAN trained over S_1 .

To prove this, we use a ground truth function that is a set-level XOR. Let every graph G_i carry a single binary feature $x_i \in \{0, 1\}$ and let the ExtGNAN encoder return this feature unchanged, i.e. $h(G_i) = x_i$. Denote a set containing two graphs by $S = \{G_1, G_2\}$ and define the permutation-invariant target

$$f_{\oplus}(S) = x_1 \oplus x_2.$$

Singleton partition (S_1). If each graph is placed in its own subset, GMAN aggregates *additively*: the model output is

$$\hat{y} = \phi(x_1) + \phi(x_2),$$

because the final GMAN stage simply sums subset scores :contentReference[0:index=0]:contentReference[1:index=1]. Write $a = \phi(0)$ and $b = \phi(1)$. To realise f_{\oplus} via a threshold τ we would need

$$a + a < \tau, \quad b + a > \tau, \quad a + b > \tau, \quad b + b < \tau.$$

Adding the first and last inequalities yields $a + b < \tau$, while the middle pair gives $a + b > \tau$ —a contradiction. Hence GMAN_{S_1} cannot represent f_{\oplus} .

Paired partition (S_2). Group the two graphs together and use a DeepSet $\Phi(S_2) = g(\sum_{i=1}^2 f(x_i))$ with $f(x) = x$ and $g(s) = s(2-s)$. Then

$$g(x_1 + x_2) = \begin{cases} 0 & (x_1, x_2) = (0, 0) \text{ or } (1, 1), \\ 1 & (x_1, x_2) = (0, 1) \text{ or } (1, 0), \end{cases}$$

exactly f_{\oplus} . The final GMAN sum over feature channels leaves this value unchanged, so GMAN_{S_2} realises f_{\oplus} .

Strict separation. Because f_{\oplus} is representable by GMAN_{S_2} but not by GMAN_{S_1} , the former is strictly more expressive.

6.3 Four-Point Condition and Recoverability

We now turn to structural identifiability. We prove that when input graphs are connected, acyclic, and positively weighted (i.e., trees), the pairwise distance matrix learned by GMAN encodes the full structure of the graph, up to isomorphism. This provides theoretical justification for the model’s ability to reason over temporal structure without needing explicit graph supervision.

The following theorem shows that if the graph satisfies the four-point condition [6], GMAN can reconstruct the original graph from the transformed distance matrix that is fed to GMAN as the graph input:

Theorem 6.1. *Let G be a graph represented by an adjacency matrix A , and D be the transformed distance-matrix for GMAN. Then if D satisfies the four-point condition, GMAN can learn ρ such that $\rho(D) = A$.*

Proof. Let $G = (V, E, w)$ be a positively weighted path graph, i.e.

$$V = \{v_1, \dots, v_n\}, \quad E = \{\{v_i, v_{i+1}\} \mid i = 1, \dots, n-1\}, \quad w(\{v_i, v_{i+1}\}) > 0.$$

Define the pair-wise distance matrix $D \in \mathbb{R}^{n \times n}$ by

$$D_{uv} = \sum_{e \in P_G(u, v)} w(e),$$

where $P_G(u, v)$ is the unique $u-v$ path in G . Then:

- (a) Tree-metric property. D satisfies the four-point condition of Buneman [6]; hence (V, D) is a *tree metric*.
- (b) Uniqueness (*no information loss*). By Buneman’s theorem the tree that realises D is unique up to isomorphism. For a path graph the only automorphism is the reversal $(v_1, \dots, v_n) \mapsto (v_n, \dots, v_1)$, so D determines G completely except for left-right orientation.
- (c) Efficient reconstruction. G can be reconstructed from D in $O(n^2)$ time:
 - i. Choose an endpoint $s = \arg \max_{v \in V} \max_{u \in V} D_{vu}$.
 - ii. Order the vertices $v_1 = s, v_2, \dots, v_n$ so that $D_{sv_1} < D_{sv_2} < \dots < D_{sv_n}$.
 - iii. Set edge weights $w(\{v_i, v_{i+1}\}) = D_{sv_{i+1}} - D_{sv_i}$ for $i = 1, \dots, n-1$.

□

7 Dataset Details

7.1 PhysioNet P12

We provide the full list of the 36 physiological signals and 3 static patient features used in our experiments.

1. Alkaline phosphatase (ALP): A liver- and bone-derived enzyme; elevations suggest cholestasis, bone disease, or hepatic injury.

2. Alanine transaminase (ALT): Hepatocellular enzyme; increased values mark acute or chronic liver cell damage.
3. Aspartate transaminase (AST): Enzyme in liver, heart, and muscle; rises indicate hepatocellular or muscular injury.
4. Albumin: Major plasma protein maintaining oncotic pressure and transport; low levels reflect inflammation, malnutrition, or liver dysfunction.
5. Blood urea nitrogen (BUN): End-product of protein catabolism cleared by the kidneys; elevation signals renal impairment or high catabolic state.
6. Bilirubin: Hemoglobin breakdown product processed by the liver; accumulation indicates hepatobiliary disease or hemolysis.
7. Cholesterol: Circulating lipid essential for membranes and hormones; dysregulation is linked to cardiovascular risk.
8. Creatinine: Waste from muscle metabolism filtered by the kidneys; higher levels imply reduced glomerular filtration.
9. Invasive diastolic arterial blood pressure (DiasABP): Pressure during ventricular relaxation; low readings may reflect vasodilation or hypovolemia.
10. Fraction of inspired oxygen (FiO_2): Proportion of oxygen delivered; values above ambient air denote supplemental therapy.
11. Glasgow Coma Score (GCS): Composite neurologic score for eye, verbal, and motor responses; scores ≤ 8 indicate severe impairment.
12. Glucose: Principal blood sugar; hypo- or hyper-glycemia can cause neurologic compromise and metabolic instability.
13. Serum bicarbonate (HCO_3): Key extracellular buffer; low levels signal metabolic acidosis, high levels metabolic alkalosis or compensation.
14. Hematocrit (HCT): Percentage of blood volume occupied by red cells; reduced values denote anemia, elevated values hemoconcentration.
15. Heart rate (HR): Beats per minute reflecting cardiac demand; tachycardia indicates stress or shock, bradycardia conduction disorders.
16. Serum potassium (K): Crucial intracellular cation; deviations predispose to dangerous arrhythmias.
17. Lactate: By-product of anaerobic metabolism; elevation marks tissue hypoxia and shock severity.
18. Invasive mean arterial blood pressure (MAP): Time-weighted average arterial pressure; low values threaten organ perfusion.
19. Mechanical ventilation flag (MechVent): Binary indicator of ventilatory support; presence denotes respiratory failure or peri-operative care.

20. Serum magnesium (Mg): Cofactor for numerous enzymatic reactions; abnormalities contribute to arrhythmias and neuromuscular instability.
21. Non-invasive diastolic arterial blood pressure (NIDiasABP): Cuff-derived diastolic pressure; trends mirror vascular tone without an arterial line.
22. Non-invasive mean arterial blood pressure (NIMAP): Cuff-based mean pressure; used when invasive monitoring is unavailable.
23. Non-invasive systolic arterial blood pressure (NISysABP): Cuff-derived systolic pressure; elevations suggest hypertension or pain response.
24. Serum sodium (Na): Principal extracellular cation governing osmolality; dysnatremias cause neurologic symptoms and fluid shifts.
25. Partial pressure of arterial carbon dioxide (PaCO₂): Indicator of ventilatory status; hypercapnia implies hypoventilation, hypocapnia hyperventilation.
26. Partial pressure of arterial oxygen (PaO₂): Measure of oxygenation efficiency; low values denote hypoxemia.
27. Arterial pH: Measure of hydrogen-ion concentration; deviations from normal reflect systemic acid-base disorders.
28. Platelet count (Platelets): Thrombocyte concentration essential for hemostasis; low counts increase bleeding risk, high counts thrombosis risk.
29. Respiration rate (RespRate): Breaths per minute; tachypnea signals metabolic acidosis or hypoxia, bradypnea central depression.
30. Hemoglobin oxygen saturation (SaO₂): Percentage of hemoglobin bound to oxygen; values below normal indicate significant hypoxemia.
31. Invasive systolic arterial blood pressure (SysABP): Peak pressure during ventricular ejection; extremes compromise end-organ perfusion.
32. Body temperature: Core temperature; fever suggests infection, hypothermia exposure or metabolic dysfunction.
33. Troponin I: Cardiac-specific regulatory protein; elevation confirms myocardial injury.
34. Troponin T: Isoform of cardiac troponin complex; rise parallels Troponin I in detecting myocardial necrosis.
35. Urine: Hourly urine volume as a gauge of renal perfusion; oliguria signals kidney hypoperfusion or failure.
36. White blood cell count (WBC): Reflects immune activity; leukocytosis suggests infection or stress, leukopenia marrow suppression or severe sepsis.

Static patient features: Age; Gender; *ICUType* – categorical code for the admitting intensive care unit (1 = Coronary Care, 2 = Cardiac Surgery Recovery, 3 = Medical ICU, 4 = Surgical ICU), capturing differences in case mix and treatment environment.

7.2 Crohn's Disease Prediction

We detail the full list of the 17 biomarkers extracted from the Danish health registries.

1. C-reactive protein (CRP): A protein produced by the liver in response to inflammation. Elevated CRP indicates active inflammation, often associated with inflammatory diseases like CD.
2. Faecal Calprotectin (F-Cal): A protein released from neutrophils into the intestinal lumen, detectable in stool samples. Elevated levels indicate gastrointestinal inflammation and are commonly used to detect and monitor inflammatory bowel disease.
3. Leukocytes (White Blood Cells): Cells that are central to the body's immune response. Elevated leukocyte counts typically suggest infection or inflammation, including flare-ups in CD.
4. Neutrophils: A type of leukocyte involved, among other things, in fighting bacterial infections. High neutrophil counts often indicate acute inflammation or infection, including intestinal inflammation in CD.
5. Lymphocytes: A group of white blood cells that form the core of the adaptive immune system, including T cells, B cells, and natural killer (NK) cells. They are responsible for antigen-specific immune responses. Abnormal levels can signal immune dysregulation, often implicated in autoimmune and chronic inflammatory diseases such as CD.
6. Monocytes: A type of white blood cell that circulates in the blood and differentiates into macrophages or dendritic cells upon entering tissues. These cells are essential for phagocytosis, antigen presentation, and regulation of inflammation. Elevated levels may reflect immune activation or tissue damage.
7. Eosinophils: Immune cells involved primarily in allergic reactions and parasitic infections. Elevated eosinophil counts might reflect allergic responses or gastrointestinal inflammation.
8. Basophils: The least common type of leukocyte, involved in allergic and inflammatory responses. Their elevation is uncommon but may accompany certain inflammatory or allergic conditions.
9. Platelets: Cell fragments critical for blood clotting and also involved in inflammatory responses. High platelet counts (thrombocytosis) are commonly seen during active inflammation in conditions like CD.
10. Hemoglobin (Hb): The protein in red blood cells responsible for oxygen transport. Low hemoglobin (anemia) is frequently observed in chronic inflammatory conditions such as CD due to blood loss or nutrient deficiencies.
11. Iron: An essential mineral for red blood cell production. Low iron levels often indicate chronic blood loss or malabsorption, both common in CD due to intestinal inflammation.
12. Folate (Vitamin B9): A vitamin necessary for red blood cell production and DNA synthesis. Deficiency may result from impaired absorption in inflamed intestinal tissue.
13. Vitamin B12 (Cobalamin): Required for red blood cell production and neurological function. Deficiencies are common in CD, especially when the ileum is affected.

14. Vitamin D2+D3 (Ergocalciferol + Cholecalciferol): Vitamins essential for bone health and immune regulation. Low levels are often seen in CD due to malabsorption and systemic inflammation.
15. ALAT (Alanine Aminotransferase): An enzyme indicating liver function. Elevated levels may reflect liver inflammation, medication effects, or co-occurring autoimmune liver disease.
16. Albumin: A protein produced by the liver that helps maintain blood volume and transport nutrients. Low albumin can reflect chronic inflammation, malnutrition, or protein loss in CD.
17. Bilirubin: A compound produced from red blood cell breakdown. It is filtered by the liver and excreted into the intestine via bile. Elevated levels may indicate liver dysfunction, bile duct obstruction, or hemolytic anemia.

7.2.1 Clinical Context and Related Work for predicting CD onset

Research on predicting the onset of CD has explored a range of approaches, including the use of routinely measured blood-based biomarkers and more complex biological data derived from multi-omics technologies.

Several studies have assessed the predictive potential of standard clinical blood tests. For example, [45] analyzed six routine biomarkers from 1,186 Danish patients eventually diagnosed with CD, achieving moderate predictive performance (AUROC of 0.74) approximately six months before clinical diagnosis. Larger-scale analyses, such as those using UK Biobank data, combined multiple standard biomarkers and basic demographic information, reporting similar predictive performances (AUROCs typically between 0.70–0.75). These analyses generally utilized methods like logistic regression, random forests, or gradient-boosted trees, favored for structured clinical datasets.

Other studies have integrated advanced biochemical data, known as multi-omics, including large-scale protein measurements (proteomics), metabolites (metabolomics), or genomic markers. [15] for instance, combined 67 blood biomarkers with approximately 2,900 plasma proteins from the UK Biobank, achieving an AUROC of 0.786. [46] combined genetic risk scores with extensive proteomic data, achieving an AUROC of 0.76 for CD prediction up to five years prior to diagnosis. Similar multi-omics approaches employing microbiome profiling, immune signaling molecules (cytokines), or lipid molecules typically achieve AUROCs between 0.75 and 0.80 but often involve significant cost, specialized laboratory analyses, and reduced consistency across diverse patient cohorts.

Overall, routine blood tests provide meaningful predictive signals for CD onset, while integrating complex biochemical measurements can improve predictive accuracy, albeit at greater cost, complexity, and variability across clinical populations.

8 Biomarker Subset Groupings

8.1 P12

In the PhysioNet P12 task, we grouped the 36 physiological signals into one multivariate subset and 29 singleton subsets. Domain knowledge showed that only the respiratory and gas-exchange variables shared sufficiently strong, coherent dynamics to benefit from joint modeling. All other signals were physiologically diverse, so they were left as singletons to retain their unique predictive information.

1. Respiratory gas exchange and ventilation

[FiO₂, PaO₂, PaCO₂, SaO₂, RespRate, pH, MechVent]

These variables collectively describe oxygen delivery (FiO₂), pulmonary gas exchange efficiency (PaO₂, SaO₂), ventilatory adequacy (PaCO₂, RespRate, MechVent), and the resulting systemic acid–base balance (pH). Grouping them lets the model learn the tightly coupled patterns that arise during hypoxemia, hypercapnia, mechanical ventilation adjustments, and respiratory failure—yielding a more coherent representation of a patient’s real-time respiratory status.

2. Singleton biomarkers

Each remaining signal represents a distinct physiological domain (hepatic, renal, hematologic, hemodynamic, neurologic, metabolic, or cardiac). Their organ-specific pathophysiology favored treating them individually, preserving granular patterns while keeping the grouping scheme simple and interpretable.

8.2 CD

In the Crohn’s Disease prediction task, we grouped the 17 selected biomarkers into 7 subsets based on shared physiological function, clinical relevance, and correlated patterns observed in exploratory analyses. This configuration produced the most robust and interpretable results, balancing domain knowledge with empirical performance. The grouping is as follows:

1. White blood cell subtypes

[Leukocytes, Neutrophils, Lymphocytes, Monocytes, Eosinophils, Basophils]

These biomarkers all represent components of the immune system’s cellular response. Grouping them enables the model to learn shared immune activation patterns, which are known to be dysregulated in inflammatory bowel diseases like CD. Combining them in a multivariate subset captures both their relative proportions and total counts, which are clinically relevant for distinguishing inflammation subtypes.

2. Inflammation markers

[CRP, Faecal Calprotectin]

These are key indicators of systemic and intestinal inflammation, respectively. CRP reflects acute-phase liver response, while F-Cal is specific to intestinal neutrophilic activity. Though mechanistically distinct, both are strongly correlated with inflammatory disease activity and complement each other in modeling CD-specific inflammation signatures.

3. Platelets

[Platelets]

Thrombocytosis (elevated platelet count) is a well-established marker of chronic inflammation. As platelet behavior is relatively independent from other hematological and nutritional markers, we model it as its own trajectory.

4. Hemoglobin

[Hemoglobin]

Hemoglobin concentration is a direct measure of anemia, which is prevalent in CD patients due to chronic blood loss and inflammation-induced iron sequestration. Its temporal dynamics often diverge from those of other blood components, warranting a separate representation.

5. Iron status

[Iron]

Iron metabolism is tightly linked to both hemoglobin levels and systemic inflammation but shows distinct dynamics. Modeling it separately allows the model to learn delayed or decoupled effects (e.g., iron deficiency preceding hemoglobin drop).

6. Vitamin and folate status

[Folate, Vitamin B12, Vitamin D2+D3]

These nutrients are absorbed in different regions of the gastrointestinal tract (e.g., B12 in the ileum, folate in the jejunum), and their deficiency profiles can be informative of CD location and severity. Grouping them allows the model to detect joint patterns of malabsorption and systemic nutrient depletion.

7. Liver function markers

[ALAT, Bilirubin, Albumin]

These biomarkers reflect hepatic function and protein synthesis. Abnormal liver enzymes and hypoalbuminemia are frequently observed in CD due to medication effects, chronic inflammation, or comorbid autoimmune liver disease. Combining them supports learning of systemic inflammatory effects beyond the gut.

This grouping reflects known biological relationships, enhances the interpretability of the model’s subset-level attributions, and improves performance compared to unstructured or purely univariate representations. It enables GMAN to exploit interactions among related features while maintaining a modular structure that aligns with clinical reasoning.

9 Experimental Setup, Hyperparameter Choices and Grouping Configurations

This section outlines key implementation choices and model settings used in our experiments, including the manually tuned biomarker grouping configurations that served as an important hyperparameter for performance and interpretability.

9.1 General Experimental Setup

9.1.1 Crohn’s Disease Experiments

Unless otherwise noted, we trained all CD models for a maximum of 300 epochs using the Adam optimizer with weight decay in the 1e-2, 1e-5 range. We used a ReduceLROnPlateau scheduler with a max learning rate in the 1e-2, 1e-4 range, min learning rate in the 1e-7, 1e-8 range, factor in the 0.2-0.9 range and patience=100

We trained all GMAN models with batch size of range 64, 256, dropout in the 0.1-0.2 range, n_layers in the 2, 10 range, hidden_channels in the 4, 64 range, num_lab_ids_embed in the 5, 8 range, num_biom_embed in the 3, 5 range, num_units_embed in the 3, 5 range.

Random seeds were fixed for reproducibility, and results are reported across three independent runs. All models were trained on a single NVIDIA Tesla V100-PCIE-16GB GPU.

9.1.2 In-Hospital Mortality (P12) Experiments

We trained all PhysioNet12 models for a maximum of 500 epochs using the Adam optimizer with weight decay of 1e-4. We used a ReduceLROnPlateau scheduler with a max learning rate in the {1e-3, 1e-5} range, min learning rate of 1e-5, factor of 0.5 and patience=20.

We trained GMAN models with batch size of range {16, 32}, dropout of 0.2, n_layers in the {3, 5} range, hidden_channels in the {32, 64} range, num_lab_ids_embed in the {5, 8} range, num_biom_embed in the {3, 5} range, num_units_embed in the {3, 5} range.

Random seeds were fixed for reproducibility, and results are reported across three independent runs. All models were trained on a single NVIDIA Tesla V100-PCIE-16GB GPU.

9.1.3 Fake-News Detection (GossiCop) Experiments

We trained all GNAM GossiCop models for a maximum of 400 epochs using the Adam optimizer with weight decay of 1e-4. We used a ReduceLROnPlateau scheduler with a max learning rate in the {1e-3, 5e-5} range, min learning rate of 1e-8, factor of 0.5 and patience=20.

We trained GMAN models with batch size of 16, dropout in {0.0, 0.5} range, n_layers in the {3, 5} range, hidden_channels in the {16, 128} range.

Random seeds were fixed for reproducibility, and results are reported across three independent runs. All models were trained on a single NVIDIA Quadro RTX 8000 (48GB) GPU.

9.2 Grouping Configurations for Clinical Tasks

In both clinical tasks, the configuration of input feature subsets (i.e., how we grouped input biomarkers into multivariate trajectories) was treated as a manually tuned hyperparameter. These groupings determine how GMAN combines individual graph representations prior to final prediction, and they affect both the expressivity and interpretability of the model.

In-Hospital Mortality (P12). We compared GMAN’s performance under the following grouping strategies:

- **All singletons** - 36 groups as the number of biomarkers.
- **Respiratory** - one group of the biomarkers: *[FiO₂, PaO₂, PaCO₂, SaO₂, RespRate, pH, MechVent]* and the rest are singletons.

- **Metabolic Electrolytes** - one group of the biomarkers: $\{Na, K, Mg, HCO_3, Lactate, Glucose\}$ and the rest are singletons.

Crohn's Disease Onset. We evaluated several grouping configurations:

- **Flat grouping:** All 17 biomarkers are modelled independently.
- **Biologically driven grouping** (see Appendix 8.2): Biomarkers are grouped into 7 clinically coherent subsets (e.g., inflammation markers, immune cell subtypes, liver function).
- **Diagnostic Panel Grouping:** A clinically motivated grouping that mirrors standard blood test panels used in routine diagnostics.
- **Data-driven grouping:** Groupings are derived from clustering biomarkers based on the complementary signal in their attribution curves (see Section 4.1.3).
- **Merged coarse groupings:** Broad categories such as inflammation, haematology, and micronutrients.
- **Minimal Pairwise Interaction :** Emphasizes minimal yet informative combinations that capture key axes of immune, inflammatory, and metabolic variational proximity.